Two-stage melting in two dimensions in a system with dipole interactions

R. E. Kusner*
Department of Physics, Case Western Reserve University, Cleveland, Ohio 44106

J. A. Mann
Department of Chemical Engineering, Case Western Reserve University, Cleveland, Ohio 44106

A. J. Dahm
Department of Physics, Case Western Reserve University, Cleveland, Ohio 44106
(Received 23 September 1994)

Two-stage melting is observed in a two-dimensional colloidal suspension with dipolar interactions. Micrometer-sized polystyrene spheres dispersed in water are confined to two dimensions between glass cover slides. Application of an ac electric field normal to the layer leads to an interparticle interaction that is to good approximation a repulsive dipole interaction. The array solidifies at large applied fields. Translational and bond-orientational correlation functions and critical exponents for the algebraic decay of these correlation functions are consistent with the dislocation-mediated melting theory of Kosterlitz, Thouless, Halperin, Nelson, and Young. The defects observed are those predicted for the crystal, hexatic, and fluid phases. The one-component plasma parameter, Γ, is found to equal 61 ± 3 at melting in agreement with computer simulations. Grain boundaries are not observed in the intermediate, hexatic phase. The bond-orientational correlation function shows a clear hexatic-to-fluid transition. The potential energy varies smoothly through the transitions between phases.

I. INTRODUCTION

Aside from surface melting, melting of a three-dimensional solid is not understood. Two-dimensional (2D) systems are more experimentally accessible for probing the phenomena of melting, and computer simulations of 2D systems are far more practical. Further, a number of theories of melting in two dimensions have been developed. One of these, the Kosterlitz-Thouless-Halperin-Nelson-Young[1-3] (KTHNY) theory of melting driven by the dissociation of dislocation pairs predicts continuous-order melting that occurs in two stages. Translational order is destroyed at the first transition and bond-orientational order at the second. The intermediate state is a hexatic phase. Thus, it is of interest to find either naturally occurring or model, 2D arrays for the study of melting and of the hexatic phase.

A. Theories of two-dimensional melting

Long-wavelength phonons destroy long-range translational order in 2D crystals.[4] Translational correlations decay algebraically, i.e., quasi-long-range order exists. However, bond-orientational order remains. Kosterlitz and Thouless[1] developed a theory in which dislocation pairs, which exist in small concentrations in the lattice, unbind and become uncorrelated at the melting temperature. This transition occurs when the free energy for a single free dislocation in the system goes to zero. This condition leads to the Kosterlitz-Thouless criterion which gives a relation between the transition temperature, T_{KT}, and the renormalized Lamé coefficients λ and μ (the shear modulus). It is

$$T_{\mathrm{KT}}=\frac{a^2\mu(\mu+\lambda)}{4\pi k_B(2\mu+\lambda)}\ , \tag{1.1}$$

where a is the lattice spacing. Halperin and Nelson pointed out that although such a transition would destroy quasi-long-range translational order, bond-orientational order would persist. Above T_{KT} a hexatic phase exists in which the bond-orientational correlations decay algebraically. At a higher temperature, T_i, dislocations, which are closely bound disclination pairs, unbind into free disclinations to form the fluid phase in which both translational and bond-orientational order are short range. The KTHNY theory described above makes many predictions which can be tested experimentally. It predicts a set of defects, dislocation pairs, free dislocations, and free disclinations, which are characteristic, respectively, of the crystal, hexatic, and fluid phases. It also predicts the form of the translational and bond-orientational correlation functions, the exponents for the respective algebraic decays, and the temperature dependence of the correlation lengths for the exponential decay of the correlations functions. The transitions are predicted to be continuous. A broad maximum is predicted in the specific heat just above the melting temperature caused by the gradual dissociation of dislocation pairs.[5] A discontinuity in the dc shear modulus, rounded at finite frequencies, to a value of zero is predicted.

Chui[6] developed a theory in which dislocation pairs would form grain boundaries and melt the solid before the dislocation-unbinding transition. The competition between random dislocations and dislocations aligned on

grain boundaries depends on the density of dislocations. Chui found a weak first-order transition for low dislocation densities, $E_c/k_BT_c > 2.84$, and a strong first-order transition for a smaller dislocation core energy, E_c. Grain-boundary melting circumvents the hexatic state. Other first-order theories have been proposed.[7–9] Glaser and Clark[10] have presented a thorough review of 2D melting theories.

Specific forms for the correlation functions are given for the hexatic phase by the KTHNY theory. The translational correlation function is defined by

$$C_{\mathbf{G}}(\mathbf{r}) \equiv \int \rho_G(\mathbf{r}'-\mathbf{r})\rho_G(\mathbf{r}')d\mathbf{r}^2 \tag{1.2}$$

where $\rho(\mathbf{G}) \equiv \exp(i\mathbf{G}\cdot\mathbf{r})$, and $\mathbf{G}$ is a principal reciprocal-lattice vector. The bond-orientational correlation function is defined as

$$C_6(\mathbf{r}) \equiv \int \Psi_6(\mathbf{r}'-\mathbf{r})\Psi_6(\mathbf{r}')d\mathbf{r}^2 \tag{1.3}$$

where $\Psi_6(\mathbf{r}) \equiv \sum_{j=1}^{\mathrm{NN}} \exp[i\theta_j(\mathbf{r})]/N_{\mathrm{NN}}$. Here N_{NN} is the number of nearest neighbors of a particle at $\mathbf{r}$, and θ_j is the angle that the jth nearest-neighbor bond makes with an external direction.

The translational correlation function decays algebraically in the crystal phase, $C_G(\mathbf{r}) \approx r^{-\eta_g(T)}$, and decays exponentially, $C_G(\mathbf{r}) \approx \exp(-r/\xi_G)$, in the hexatic and fluid phases. The bond-orientational correlation function decays to a finite value in the crystal phase, decays to zero algebraically with an exponent $\eta_6(T)$ in the hexatic phase and exponentially in the fluid with a correlation length ξ_6. The predicted values of the algebraic exponents at the crystal-to-hexatic and hexatic-to-fluid transitions are, respectively, $\eta_G \approx \frac{1}{3}$ and $\eta_6 = \frac{1}{4}$.

B. Computer simulations

Nearly all computer simulations of 2D melting indicated a first-order transition.[11] Specifically, for dipole interactions of interest here, Kalia and Vashishta,[12] and Bedanov, Gadiyak, and Lozovik[13,14] found a first-order transition. It is of significance that the latter group found two-stage melting consistent with the KTHNY theory for a Coulomb interaction and first-order melting for dipole and Lennard-Jones interactions. These simulations gave an entropy discontinuity[15] of $0.3k_B$ at a value of the plasma parameter $\Gamma = V(r_s)/k_BT_m = 62 \pm 3$ Here $V(r_s)$ is the interaction potential at the Wigner-Seitz radius. Using density-functional techniques Ramakrishnan[7] also found an entropy discontinuity of $0.32k_B$ at the melting transition.

C. Experimental tests of two-dimensional melting

A number of systems with different potentials have been probed. Extensive reviews of these systems have been given by Strandburg[11] and Murray.[16] The simplest system of 2D particles consists of a layer of electrons supported by a liquid-helium surface. In this system Deville *et al.*[17] measured a sharp decrease in the finite-frequency shear modulus at melting, and Glattli, Andrei, and Williams[18] determined an upper limit of $0.2k_B$ for the latent heat of melting. Jiang and Dahm[19] studied melting of electron crystals on helium films where the shear modulus is weakened due to screening by a dielectric substrate. Melting followed the Kosterlitz-Thouless criterion through a wide range of shear moduli. These observations provide strong support for dislocation-mediated melting. Stan and Dahm[20] measured a smooth variation of the electron effective mass through the transition and a sharp peak in the electron-ripplon scattering crosssection near the transition. They interpreted these results in terms of the dislocation unbinding model.

Murray and co-workers[21,22] have carried out an extensive study of a model system comprised of monodispersed, charged, polystyrene spheres in water interacting via a screened Coulomb potential. The spheres were confined between two glass plates in a wedge geometry. The system was studied with video microscopy as a function of density which increased with the spacing of the plates. They observed two-stage melting consistent with the KTHNY theory. Armstrong, Mockler, and O'Sullivan[23] examined two systems of polystyrene spheres at the air-water interface. An array of 2.88-μm spheres showed evidence of defect-mediated melting and a hexatic state, while a sample of 1.01-μm spheres showed no hexatic state. Its melting evolved with a different defect structure. Tang *et al.*[24] studied the free expansion of 1.01-μm polystyrene sphere dispersed in water and confined between glass plates. While a two-stage process was observed, the defect structure was more consistent with a first-order transition since dislocations clearly aggregated into strings in the transition region. It is unclear whether the differences in the observed melting processes among the colloidal systems result from different interparticle potentials or equilibration problems in the systems with larger spheres. Finally a number of Lennard-Jones systems of adsorbed atoms have been probed.[11,25] In these systems the substrate imposes a periodic potential on the particles. While some of the data have been interpreted in terms of a KTHNY transition, a specific-heat jump at the transition has been observed in some of these systems.[26]

Three other artificial systems have been studied. Skjeltorp[27] probed 1.9-μm polystyrene spheres dispersed in a ferrofluid between two glass plates with a magnetic field applied normal to the layer. These "voids" in the ferrofluid interacted with a magnetic dipole interaction. The system melted as the field strength was reduced at a value of Γ consistent with the molecular-dynamics simulation of Kalia and Vashishta. In this experiment and another by Helgesen and Skjeltorp[28] on an array of rotating pairs of polystyrene spheres, disorder in the lattice grew in from grain boundaries which were present in the initial crystal.

Seshadri and Westervelt[29] studied a magnetic bubble array in a thin film of magnetic garnet. These magnetic domains interacted via a dipole potential. Thermal motion was simulated by agitating the bubbles with an ac magnetic field. Their system formed a hexatic glass at large Γ values due to pinning of the domains. A continuous transition to the fluid state was observed.

We present here a study[30] of melting in a 2D array of monodispersed colloidal particles interacting via a dipole potential. It is the electrical analog of Skjeltorp's system. A shorter summary of our work has been presented elsewhere.[31]

II. EXPERIMENTAL SYSTEMS AND ANALYSIS

A. The colloidal monolayer cell

In this experiment we study ordering of electrically polarized, monodispersed, micrometer-sized colloids confined to a plane. The colloid is a spherical, monodispersed, polystyrene latex with sulfonate (SO_4^-) surface groups. These colloids, obtained commercially,[32] are dispersed in water at a $\sim 10\%$ volume fraction. Data from 1.6- and 2.0-μm particles are presented below. The standard deviations of the particle sizes did not exceed 2% of the particles diameters. Both batches had a concentration of sulfonate groups of about 2×10^{13} cm^{-2} on each particle.

Shown schematically in Fig. 1, the colloid is confined between two 150-μm-thick microscope coverslips (Corning glass 0211), each of which is laminated to a sapphire window for support and thermal conduction. An EPDM *O* ring hermetically seals the colloid between the two windows. This assembly is placed in the center of an aluminum jig with three differential micrometers positioned at 120° from each other with respect to the center. The micrometers compress the *O* ring, sealing the cell and aligning the coverslip surfaces parallel to a separation of about $1\frac{1}{2}$ particle diameters.

A 200-Å thick film of Au between the sapphire and coverslip serves as the transparent electrode for the electric field which polarizes the colloid and induces a dipole interparticle potential. An electric field at a frequency of 3.75 MHz is applied by these electrodes to prevent screening by ions in the water. The electrodes are not placed in contact with the colloid to prevent the colloid from sticking to the confining surfaces. The confining glass surfaces repel the colloid due to OH-groups found on their surface in water and due to like image charges from the glass-water interface. This stabilizes the particles between these surfaces. Field gradients at the edges of the transparent electrodes confine the particles radially.

Cleanliness is of paramount importance in the assembly of the cell, as any impurities may cause the colloid to flocculate or stick to the glass surfaces. All glass and sapphire components are heated in a sulfuric/nitric acid mixture (3:1) to oxidize any organic residue on the surface to remove it. Polymer and metal components (the *O* ring, and the hypodermic needle used to inject the colloid) are heated in a detergent and then repeatedly rinsed with distilled water. They are then ultrasonically agitated in methanol to remove organic residue. Next, all components are repeatedly rinsed and heated in filtered, deionized water (18 MΩ cm, 72 dynes/cm) from a Millipore system. Just before assembly, the coverslips and the sapphire are held over steam and then blown free of any condensate. After assembly, the confining surfaces of glass and sapphire are exposed to short-wave UV light (185 and 254 nm) to remove any remaining organic residue.[33] Finally, the surfaces are exposed to steam, blown dry, and sealed with an *O* ring. The entire process described above is performed in a class 100 clean room.

As received, the colloid has a slight tendency to aggregate and stick to glass surfaces. Using a technique developed at the University of Colorado,[34] the colloidal particles are washed repeatedly in methanol and then redispersed in water. This is accomplished by spinning the particles out of suspension with a centrifuge, decanting the supernatant, refilling the sample tube with fresh solvent, and then redispersing the particles with ultrasonic agitation. After resuspending the particles about ten times in HPLC grade methanol and then four times in the filtered, deionized water, the problem of aggregation and sticking is mostly alleviated.

B. Calculation of the sphere-sphere interaction

A dielectric sphere embedded in a medium of higher permittivity will produce a dipole field, centered about the sphere, in response to a uniform electric field applied far away. The associated dipole opposes the applied field

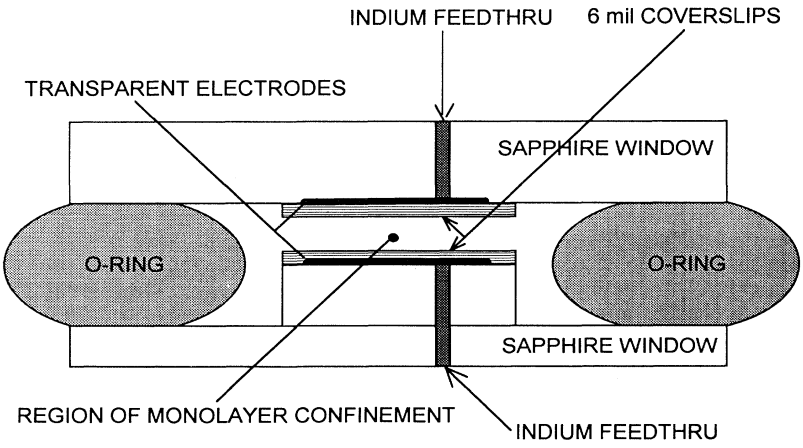

FIG. 1. Schematic cross section of colloidal monolayer cell.

with strength[35]

$$\mathbf{p}_s = -\varepsilon_f \frac{(\varepsilon_f - \varepsilon_s)}{(2\varepsilon_f + \varepsilon_s)} r_0^3 \mathbf{E}_f \ , \tag{2.1}$$

where the subscript f refers to the medium, a fluid in this experiment, s to the sphere, and r_0 refers to the radius of the sphere. This induced dipole feels no force from the uniform field; however, it will be stressed by other dipoles. Ignoring as small the fact that the two polarized spheres will induce dipoles and multipoles in each other, the potential energy associated with the interaction between two spheres can be derived from that of two dipoles in a dielectric medium. Analogous to the Coulomb energy in a dielectric medium, the dipole energy is

$$V(\mathbf{r}_1 - \mathbf{r}_2) = \frac{1}{\varepsilon_f} \left\{ \frac{\mathbf{p}_1 \cdot \mathbf{p}_2}{|\mathbf{r}_1 - \mathbf{r}_2|^3} - 3 \frac{\mathbf{p}_1 \cdot (\mathbf{r}_1 - \mathbf{r}_2) \mathbf{p}_2 \cdot (\mathbf{r}_1 - \mathbf{r}_2)}{|\mathbf{r}_1 - \mathbf{r}_2|^5} \right\} . \tag{2.2}$$

Applying the results of (2.1), assuming the dipoles lie in the same plane, normal to the dipole direction, the dipole-dipole energy becomes

$$V(r) = \varepsilon_f \frac{(\varepsilon_f - \varepsilon_s)^2}{(2\varepsilon_f + \varepsilon_s)^2} \left[\frac{r_0}{r} \right]^3 r_0^3 E_f^2 \ . \tag{2.3}$$

It is assumed that this potential produces the dominant force between particles; the screened Coulomb, and van der Waals forces are negligible for the given particle configurations when a sufficiently strong electric field is applied. This assumption is supported by the observation of particle configurations after the electric field is turned off. Then the particles approach each other and fall into the secondary potential minimum at about 1000 Å created by the competition between the repulsive screened Coulomb potential and the attractive van der Waals interaction. At the potential minimum, the van der Waals contribution to the potential is estimated to be no more than $10 k_B T$. The absolute magnitude of the screened Coulomb potential is roughly the same or smaller (the net force is zero). Consequently, at the nominal particle separation of three particle diameters, we estimate magnitude of the screened Coulomb potential to be less than $k_B T$ and that of the van der Waals interaction to be less than 0.05 $k_B T$ compared to 60 $k_B T$ for the dipole interaction at melting.

One complication in calculating the interparticle potential is screening from ions in the water. While we have insufficient knowledge of the electrochemistry to accurately determine the extent of this screening, it is assumed that these affects are linear. Consequently, the induced potential between particles remains dipole, although with a somewhat smaller magnitude than given by (2.3), and the magnitude should scale as the square of the applied field.

C. Data analysis

1. Image digitization and particle coordinate extraction

The imaging of the colloidal monolayer is straightforward. Transmitted light microscopy, using a 32 X, extra long working distance objective, produces a clear image of the monolayer. After further magnification by a variable zoom (5–12 X) the image is projected on a CCD camera. The outgoing video signal is then recorded on videotape for subsequent evaluation.

The videotaped images are analyzed by digitizing each to a 640×480 pixels array with a 256-level gray scale resolution. The spatial resolution of the digitized image ranges from 0.25 to 0.65 μm per pixel for the magnifications stated above. The resolving power of the optics is about 1.5 μm. This is sufficient to discriminate the 30-some particles across the field of view.

From this digitized image, 1000–2000 particle coordinates are extracted as follows. Since the intensity profile centered around a single particle is convex, the digitized image is convolved with a parabolic kernel to find where the image is locally convex. Specifically, the convolution is

$$I'_{m,n} = \sum_{i=-2}^{2} \sum_{j=-2}^{2} I_{m-i,n-j} k_{i,j} \ , \tag{2.4}$$

where $I_{m,n}$ is the intensity of the original image at pixel (m,n), and $I'_{m,n}$ is the convolved image. The parabolic kernel $k_{i,j}$ is given by

$$k_{i,j} = i^2 + j^2 - 4 \ . \tag{2.5}$$

The resultant image $I'_{m,n}$ is searched for local maxima, which are assumed to be the particle centers. After visually inspecting and editing for obvious errors, the array of the particle coordinates is saved for further analysis.

2. Triangular and defect identification

To analyze defects in the particle ensembles, a Delauney[36] triangulation of the points is constructed. This consists of a set of nonintersecting lines connecting nearest neighbors. For a lattice without defects each particle is connected to six nearest neighbors. A disclination results in a single five- or sevenfold-coordinated point at the core of the disclination, surrounded by sixfold vertices. The core of the dislocation consists of a five–sevenfold disclination pair. Thus, the Delaunay triangulation produces a one-to-one correlation between non-sixfold-coordinated points and defects, making defect identification easy.

3. Calculation of the bond-orientational and translational order field

The bond angles with respect to a reference axis are computed from the triangulation. From this, one can compute a complex value at each particle given by

$$\Psi_6(\mathbf{r}) = \frac{1}{N_{\mathrm{NN}}} \sum_{j \in \mathrm{NN}} e^{i 6 \theta(\mathbf{r} - \mathbf{r}_j)} \ , \tag{2.6}$$

where $\theta(\mathbf{r}-\mathbf{r}_j)$ is the bond angle of the nearest-neighbor pair with respect to the reference axis, N_{NN} is the number of nearest neighbors, and the sum is over the nearest neighbors. This function is defined only at discrete points in the plane. To create a continuum function, the values of the points within a triangle of the triangulation are linearly interpolated from the values at the triangulation vertices, where (2.6) is defined.[37] The real and imaginary components are interpolated separately. The result is the continuum bond-orientational field, from which its autocorrelation function can be computed.

The data used suffer from a density gradient across the field of view. To calculate the correlation of the displacement field due to thermal excitations, the displacement due to the density gradient must be subtracted out. An approximate expression for the displacement field of the density gradient is derived from the local values of the nearest-neighbor area, $A(x,y)$. This is calculated for each particle by summing the areas of the triangles defined by the particle's nearest neighbors. These data are then fit to the following linear model:

$$A(x,y)=A_0+ax+by \ . \tag{2.7}$$

Since the trace of the strain tensor is equal to the fractional change in local area, the following identification is made:

$$\frac{\partial \bar{u}_x}{\partial x}+\frac{\partial \bar{u}_y}{\partial y}=\frac{ax+by}{A_0} \ , \tag{2.8}$$

where $\bar{\mathbf{u}}(\mathbf{r})$ is defined as the displacement field due to the density gradient. From Eq. (2.8) the displacement field is determined, less two constants of integration. With the inclusion of two constraints, first that the displacement does not shear the lattice,

$$\frac{\partial \bar{u}_x}{\partial y}+\frac{\partial \bar{\mu}_y}{\partial x}=0 \ , \tag{2.9}$$

and second that the area expansion is isotropic,

$$\frac{\partial \bar{u}_x}{\partial x}=\frac{\partial \bar{u}_y}{\partial y} \ , \tag{2.10}$$

an approximation for the displacement field is found,

$$\bar{u}_x(x,y)=\frac{a}{4}x^2+\frac{b}{2}xy-\frac{a}{4}y^2, \tag{2.11}$$

and

$$\bar{u}_y(x,y)=-\frac{b}{4}x^2+\frac{a}{2}xy+\frac{b}{4}y^2 \ . \tag{2.12}$$

To calculate the translational order field we define a set of values at the particle positions r,

$$\rho_{\mathbf{G}}(\mathbf{r})=e^{-iG(\mathbf{r}-\bar{\mathbf{u}}(\mathbf{r}))} \ . \tag{2.13}$$

The primary reciprocal-lattice vector, $\mathbf{G}$, is found from the maxima of the structure factor of the set of particle coordinates computed by fast Fourier transform (FFT).[38] After the discrete values of Eq. (2.13) are calculated, the values are interpolated to fill a 512×512 complex array. This complex array is assumed to be a representation of the translational order field.

4. Calculation of correlation functions

The calculation of correlation functions from the digitized images is complicated by the fact that the images are finite in size, about 30–50 times larger than the interparticle distance. We are interested in the correlation functions of fields of infinite extent. To address this problem, the calculated autocorrelation functions, with prototype

$$\tilde{C}_f(x,y)=\sum_{i=x}^{M}\sum_{j=y}^{N} f^*(i,j)f(i-x,j-y) \ , \tag{2.14}$$

must be normalized at every separation to account for the area over which the sum is performed to produce a representation of the infinite space correlation function,

$$C_f(x,y)=\frac{1}{(M-x)(N-y)}\tilde{C}_f(x,y) \ . \tag{2.15}$$

Here M and N are, respectively, the width and height of the digitized image in pixels.

Application of the fact that the autocorrelation of a function $f(\mathbf{r})$ is equal to the Fourier transform of its structure factor, increases the speed of the calculation by employing the optimal FFT method. The process is given below. First the structure factor is calculated,

$$S(\mathbf{k})=|F[f(\mathbf{r})]|^2 \ , \tag{2.16}$$

where $F[\ ]$ is the fast Fourier transform. Then the correlation function is calculated from the inverse transform of $S(\mathbf{k})$,

$$\tilde{C}_f(\mathbf{r})=F^{-1}[S(\mathbf{k})] \ . \tag{2.17}$$

To prevent wraparound, the FFT must be calculated over a space twice as wide as the width of the defined field.[39] The field is extended by padding it with zeros. This correlation function, equivalent to (2.14), must be normalized as described in Eq. (2.15).

The density-correlation function is calculated most quickly by directly counting the number of particles separated by a given vector, i.e., creating a histogram of pairs with respect to the vector of separation. To produce the infinite space correlation function, this is then normalized at each separation vector by the number of pairs expected for that vector in a uniform distribution of points in the same finite area. Specifically this normalization denominator is given by

$$\rho(M-x)(N-y) \ , \tag{2.18}$$

where ρ is the density of the image, M is the width of the image in the x direction, x is the x component of the vector, N is the height of the image in the y direction, and y is the y component of the vector. The density is calculated from the reciprocal of the average nearest-neighbor area, the constant term in Eq. (2.7). This provides a truer measure of density than simply counting the number of particles in an image.

5. Calculation of the potential energy

For a pair-wise additive potential, the potential energy can be calculated from the pair density distribution func-

tion $g(r)$ as follows:

$$\frac{U^{ex}}{N}=\frac{\rho}{2}\int V(\mathbf{r})g(\mathbf{r})d^2r\ , \tag{2.19}$$

where ρ is the number density, N is the number of particles in the system and $V(\mathbf{r})$ is the pair potential. For this system, the pair potential is approximately an inverse cube potential. Since the magnitude of this potential is not known due to uncertainty about the physical parameters determining the strength of the induced dipole moment, the magnitude of the potential energy cannot be calculated. However, the ratio of the potential energy per particle to the pair potential energy at the Wigner-Seitz radius,

$$r_s=(\pi\rho)^{-1/2}\ , \tag{2.20}$$

can be determined since the magnitude of the pair potential is canceled out, with the result

$$\frac{U^{ex}}{NV(r_s)}=\frac{1}{2\sqrt{\pi^3\rho}}\int\frac{g(\mathbf{r})}{|\mathbf{r}|^3}d^2r\ . \tag{2.21}$$

This cancellation is a consequence of a simple power-law potential. If the interparticle potential were more complicated, like the screened Coulomb or Lennard-Jones potentials, this cancellation would not occur. It should be noted that for particles in a perfect triangular lattice this has the approximate limiting value 0.7985.

One complication arising from the calculation of the potential energy is that the density-correlation function is not known past the width of the image, about twenty lattice spacings. Here we assume that the correlation has a constant value of one, the density correlation for an ideal gas. This should be a fair approximation even in the solid phase due to the algebraic decay of the translational order field.

III. EXPERIMENTAL RESULTS

The melting of two different colloidal monolayer samples is presented below. The first sample consisted of 1.6-μm polystyrene spheres dispersed in water. The initial interparticle separation of the monolayer was three particle diameters. An 800-V potential at 3.75 MHz was applied across the sample for the duration of the melt. Neglecting screening by ions in the water, this corresponds to a field of 1900 V/cm. The initial state of the sample was an ordered solid. Due to the unbalanced intrinsic pressure from the induced interparticle potential, the particles slowly drifted apart at a rate of 7.5 Å/sec, weakening the interparticle potential, and ultimately causing the monolayer to melt into an isotropic liquid. This motion also caused the particles to drift across the field of view at three lattice spacings per minute. This process, from the initial signs of melting in the solid to the formation of the isotropic liquid, spanned 45 min.

Figure 2, images A–F, shows Delauney triangulations of the 1.6-μm monolayer at various stages in the melting process. The phase of each image is determined by the correlations shown in Figs. 3 and 4. Image A shows the monolayer in the 2D solid state. Several dislocations, marked by moderately shaded triangles, are present in the image. The majority of these are paired with an opposing dislocation nearby. Those unpaired dislocations are near the edge, and probably paired with dislocations just outside the field of view. Image B shows the mono-

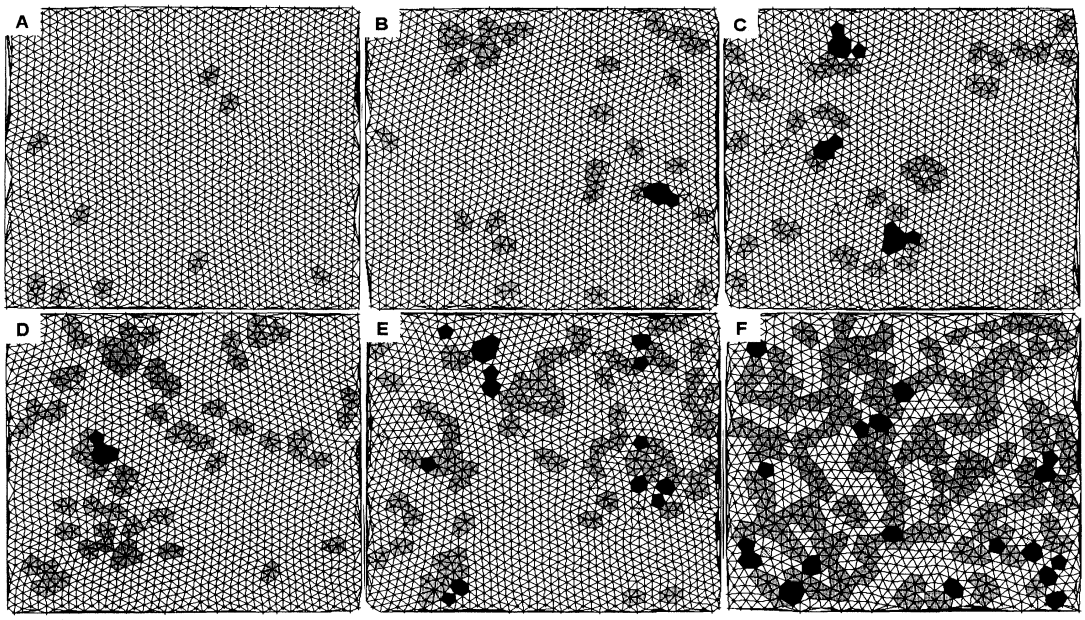

FIG. 2. Triangulations for the 1.6-μm sample at various values of Γ^*: A $\Gamma^*=1.0$; B $\Gamma^*=0.96$; C $\Gamma^*=0.91$; D $\Gamma^*=0.87$; E $\Gamma^*=0.81$; F $\Gamma^*=0.55$. Defects are labeled as heavily shaded areas, disclinations; medium shaded areas, dislocations; lightly shaded areas, paired dislocations at zero separation.

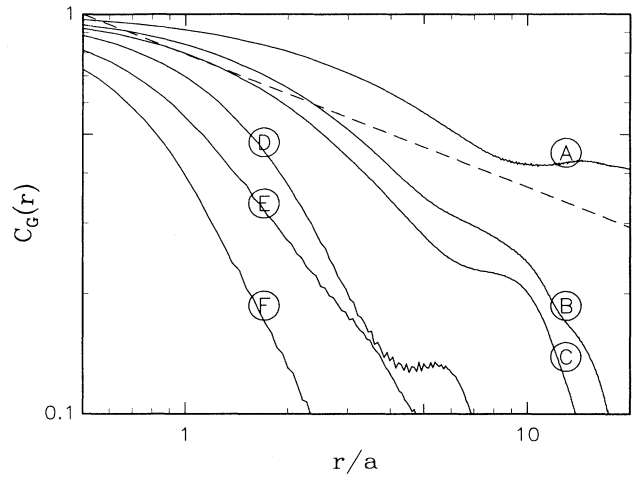

FIG. 3. Translation correlation functions. Curves are lettered to correspond to those in Fig. 2. The dashed line has a slope of $-\frac{1}{3}$.

layer with defects consistent with the hexatic phase. An increase in the density of aggregated and isolated dislocations is observed. The dark shaded region is a disclination pair. The lightly shaded region to the right of the dark region marks the formation of a virtual dislocation pair which is simply eliminated by redrawing two pairs of nearest neighbors. Image C shows the monolayer well into the hexatic phase. Dislocations, dislocation loops, disclination pairs, and virtual dislocations are present. Image D is that of the monolayer right before the hexatic-to-isotropic transition. It differs from C only in that the defect density is higher; the same types of defects are present. Image E shows the monolayer just into the isotropic liquid. Disclination pairs are separating from each other leading to the loss of orientational order. Image F shows the monolayer well into the isotropic liquid state. The density of dislocations has increased significantly so that defects percolate through the sample.

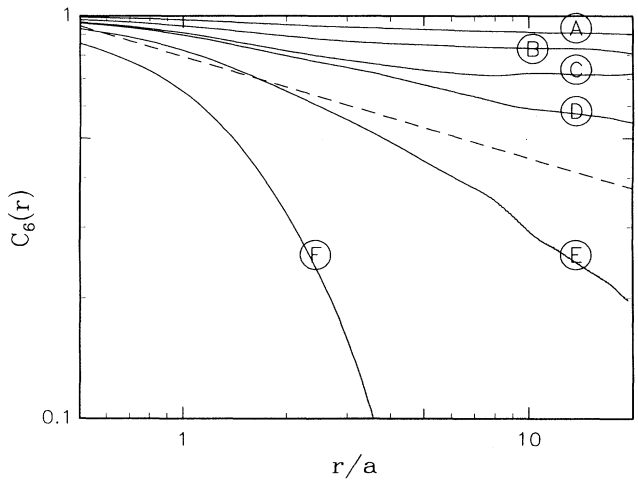

FIG. 4. Bond-orientational correlation functions. Curves are lettered to correspond to those in Fig. 2. The dashed line has a slope of $-\frac{1}{4}$.

Figure 3 shows the translational correlation function for images A–F in Fig. 2. The correlations are displayed on a log-log graph so that an algebraic decay, $C(\mathbf{r}) \propto |\mathbf{r}|^{-\eta}$, is displayed as a straight line. The correlation function for each image is labeled with the appropriate letter. The dashed line is $r^{-1/3}$, the limiting form of algebraic decay for the translational correlation function at the solid-to-hexatic transition. Only correlation function A is above and approximately asymptotic to it. The other correlation functions diverge from this line at large r indicating a exponential loss of translational order.

Figure 4 shows the bond-orientational correlation functions for the images in Fig. 2. The dashed line in this graph is $r^{-1/4}$, the limiting form of algebraic decay at the hexatic-to-isotropic fluid transition. Correlations for images A–D decay slower than this limit, indicating the presence of a bond orientationally ordered system. Correlations for images E and F decay faster than the limiting form for orientational order and, in fact, diverge from it, indicating exponential decay of this order and the existence of an isotropic fluid.

A collection of bond-orientational correlation functions from many images was presented in Fig. 3 of Ref. 31 for the sample analyzed above. This figure showed a clear break in the form of the correlation functions with an algebraic decay for $\eta > -\frac{1}{4}$ and an exponential decay just below the correlation functions that appear asymptotic to this limiting form, $r^{-1/4}$.

The calculated reduced potential energy of the system versus the effective temperature is shown in Fig. 5. The reduced potential energy, E^*, is given by Eq. (2.21). Since the real temperature of the experiment is fixed, the effective temperature is derived from the reciprocal of the one component plasma parameter Γ. This effective temperature is then normalized so that $T^*=1.0$ corresponds to the loss of translational order, as determined by the correlations shown in Fig. 3. The loss of bond-orientational order occurs approximately at $T^*=1.15$. The region in the vicinity of $T^*=1$ is expanded in the inset. The energy rises sharply in this hexatic region between $T^*=1.0$ to 1.15, and no obvious discontinuity is present. The dashed line is the reduced energy versus temperature data from a molecular-dynamics calculation of 2D dipoles by Kalia and Vashishta.[12] The arrows in this figure indicate the presence of hysteresis in the simulation from heating (the up arrow) and cooling (the down arrow) the system.

The defect density versus effective temperature and the reduced potential energy versus defect density are shown in Figs. 6 and 7, respectively. The defect density is defined as the fraction of non-sixfold-coordinated particles. Figure 7 shows a change in slope at a defect density of about 5%, above which the potential energy increases more slowly with increasing defect density. At a defect density of 20% a change in behavior is noted in both figures. After this, the defect density changes more slowly with increasing temperature, and the potential energy increases faster with increasing defect density. This

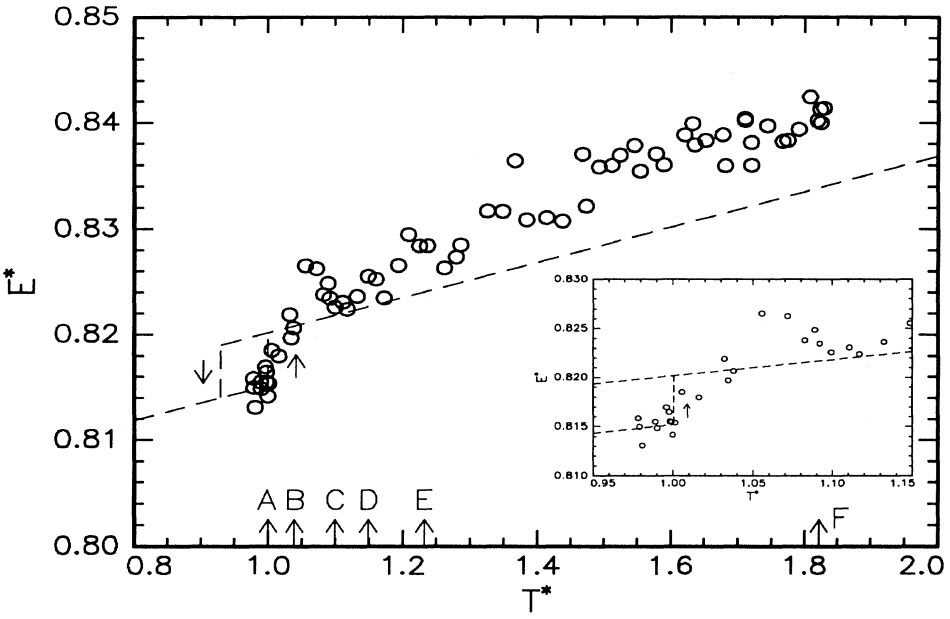

FIG. 5. Normalized potential energy versus normalized temperature for the 1.6-μm sample. Letters refer to the frames in Fig. 2. The dashed lines represent data from a molecular-dynamics simulation (Ref. 12). The inset is an expansion of the data in the vicinity of $T^*=1$.

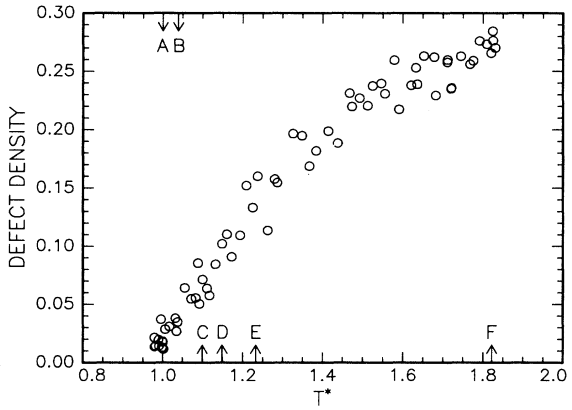

FIG. 6. Defect density versus normalized temperature. Letters refer to the frames in Fig. 2.

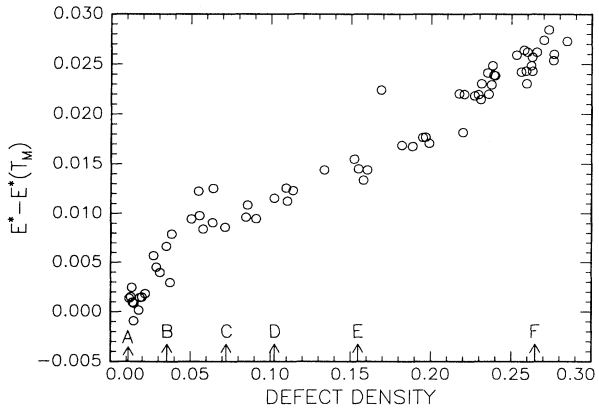

FIG. 7. Normalized potential energy versus defect density. Letters refer to the frames in Fig. 2.

occurs somewhere between images E and F in Fig. 2, where dislocations finally percolate throughout the array.

Images from a monolayer of 2.0-μm polystyrene spheres dispersed in water were also collected as they melted. The initial state of this monolayer had a particle spacing of 3.5 particle diameters. Initially a voltage of 800 V at 3.75 MHz was applied across the monolayer. This was reduced seven times by 50 V until the monolayer melted to an isotropic liquid. The monolayer also spread during this period which contributed to a reduction of the interparticle potential. This spreading averaged 3 Å/sec over the 30 min melting interval starting with the loss of translational order and ending with the loss of bond-orientational order. During this period the monolayer drifted across the field of view at a rate of three lattice spacings per minute.

Figure 8 shows six triangulations of the monolayer at various stages of melting. The shading scheme is the same as in Fig. 2: dark shaded regions are disclinations, medium shaded regions are dislocations, and lightly shaded regions are virtual dislocation pairs. Image A shows the monolayer in the translationally ordered state. The cluster of dislocations near the center of the image is a dislocation triplet, three dislocations whose Burger's vectors sum to zero. The cluster to its right also forms a triplet. Images B and C are of the monolayer in a bond orientationally ordered, yet translationally disordered state. Images D, E, and F show the monolayer with decreasing bond-orientational order in the isotropic state. The translational and bond-orientational correlation functions for these images are shown in Figs. 9 and 10, respectively. The dashed lines, as in Figs. 3 and 4, are the limiting forms for algebraic decay for the respective correlation functions. Finally, Fig. 11 shows the potential energy versus effective temperature for this monolayer.

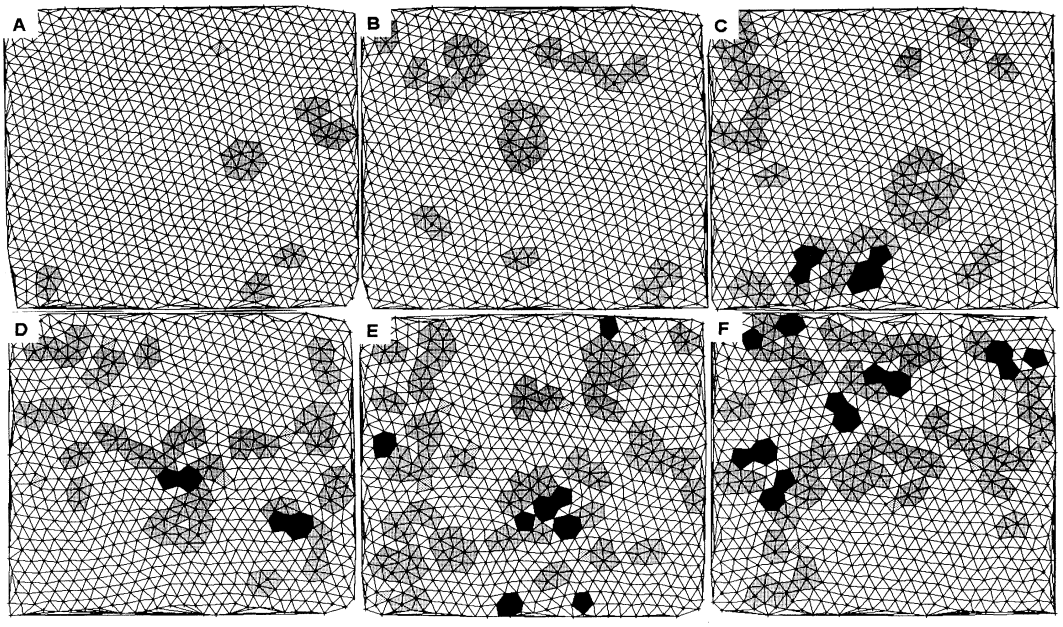

FIG. 8. Triangulations for the 2.0-μm sample at various values of Γ^*: A $\Gamma^*=1.34$; B $\Gamma^*=1.05$; C $\Gamma^*=0.80$; D $\Gamma^*=0.76$; E $\Gamma^*=0.59$; F $\Gamma^*=0.56$. Defects are labeled as heavily shaded areas, disclinations; medium shaded areas, dislocations; lightly shaded areas, paired dislocations at zero separation.

IV. DISCUSSION

The most effective technique for observing the melting of the 2D dipole system was to set the voltage, and hence the dipole strength, at a fixed value and allow the monolayer to relax to its equilibrium density distribution. This equilibrium configuration consisted of a rarified center surrounded by a dense ring of particles at the edges of the transparent electrode, where the gradients in the fringing fields confined the particles. Since the density gradients were large near the edges of this region it was necessary to observe the system near the center where density gradients were smallest, about 0.1% per lattice spacing. Since the system always rarefied over time in this region, it made no sense to change the field to reduce interparticle forces; the slow but steady increase in particle separation would do this, allowing an almost continuous study of the melting process. Unfortunately, this technique was not applied to the 2.0-μm sample, an earlier attempt at this experiment. Consequently, there are some conspicuous gaps in the melting process for this run.

The major criterion for determining the state of the system from the image was the form of the two correlation functions. It should be noted that each correlation function is calculated from a single image rather than an ensemble of images. While this certainly will introduce error into the calculated correlations, they clearly show a trend. This is especially the case for the bond-

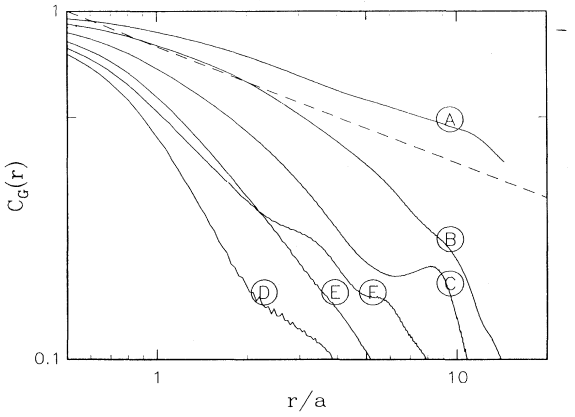

FIG. 9. Translation correlation functions. Curves are lettered to correspond to those in Fig. 8. The dashed line has a slope of $-\frac{1}{3}$.

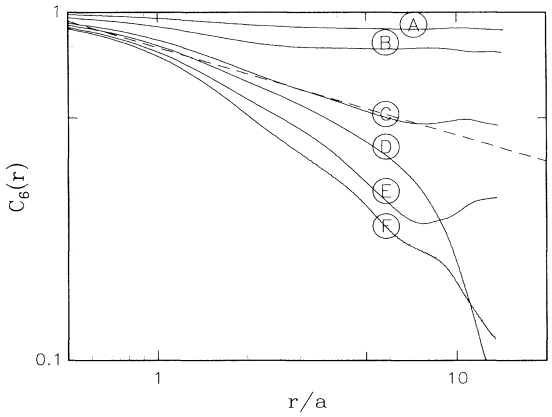

FIG. 10. Bond-orientational correlation functions. Curves are lettered to correspond to those in Fig. 8. The dashed line has a slope of $-\frac{1}{4}$.

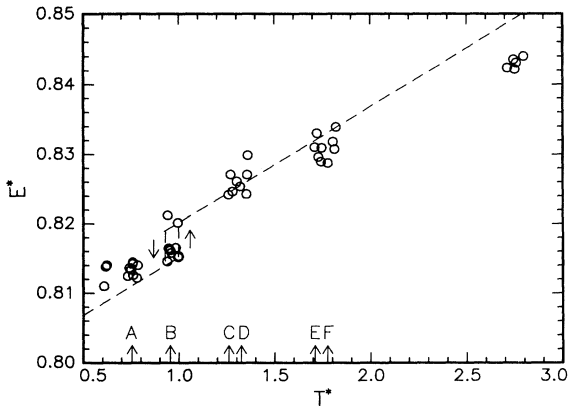

FIG. 11. Normalized potential energy versus normalized temperature for the 2.0-μm sample. Letters refer to the frames in Fig. 8. The dashed lines represent data from a molecular-dynamics simulation (Ref. 12).

orientational correlations shown in Fig. 3 of Ref. 31 which clearly shows a change in behavior from algebraic to exponential decay at $r^{-1/4}$, the predicted form of the correlation at the limit of stability for the bond-ordered phase.

The solid-to-hexatic transition is not as clearly defined by the correlation functions. Although the bond-orientational correlations appear to decay little, it is impossible to discern the transition from long-range order to quasi-long-range order on this distance scale. No clear change in the translational correlation function, such as that in Fig. 3 of Ref. 31, is seen, probably due to density gradients caused by the expansion destroying translational order and the lack of data for a well ordered solid. Also, it is questionable whether the monolayer was in equilibrium in the initial state.

The correlation functions provide evidence of the existence of the hexatic phase for this system. In both samples there are images which show a strong decay of translational order, yet only a weak algebraic decay of bond-orientation order. Since both samples evolved from a state with some translational order, very near that for a crystal at the limit of stability, it is apparent that they have lost translational order, presumably due to the formation of dislocations, as these are the only defects present in these images. It is also apparent, even from the triangulations, that bond-angle order is not lost. The existence of bond-orientational order with translational disorder is evidence of a hexatic phase. The width of the hexatic phase was 15% of T_m for the 1.6-μm sample and $\sim$25% for the 2.0-μm sample.

The images support the conclusion, drawn from the correlation functions, that there is an intermediate phase between the crystal and isotropic liquid. Images of the sample in the solid phase, Figs. 2 and 8, image A, show few dislocations, and most of those present are paired with a nearby dislocation of opposite direction. A few unpaired dislocations exist near the edges, but these are quite possibly paired with dislocations just outside the field of view. These defects are consistent with a high-temperature crystal; a few dislocations exist, but are paired over relatively short distances. Images in the hexatic phase, Fig. 2, images B–D and Fig. 8, images B and C, show the presence of more dislocations scattered more or less uniformly throughout the images and a few closely bound disclination pairs. No large aggregates of dislocations exist as predicted by Klienert's theory.[8] No obvious grain boundaries have formed either as anticipated by Chui.[6] It is plausible that small-angle grain boundaries are forming from widely separated dislocations, but this has been stated to be equivalent to dislocation unbinding.[40] Moreover, this hexaticlike behavior occurs over a large range of particle densities. One would expect a more significant change in defect structures if a first-order phase transition had occurred. The images in the fluid phase show a breakup of the previously tightly bound disclination pairs and the formation of aggregates of dislocations. The existence of a hexatic phase and the defect structures from both samples offer evidence of KTHNY melting.

The potential energy provides further insight into the melting process. In Fig. 5, the potential energy shows a fast, but apparently continuous, rise right after the solid-to-hexatic transition. This is expected from work done on the specific heat of the X-Y model which shows that the specific heat peaks above the transition.[5] A discontinuity in the calculated energy cannot be ruled out by the precision of the data, estimated to be ± 0.001 in the vicinity of the transition. This error was determined by the spread of the calculated energy at a given reduced temperature. These data are compared with data from the molecular-dynamics calculation with a r^{-3} interaction of Kalia and Vashishta[12] shown by a dashed line. Since they had calculated the total energy of the system, we subtracted one $k_B T$ from their results to obtain the potential energy. Both our data and theirs indicate a transition from the solid at $E^*=0.815$. While their potential-energy data jump discontinuously by 0.005, ours apparently spanned this energy continuously over a temperature range of 5% of T_m. They interpret this discontinuous change to be a sign of a first order transition; we interpret the apparent continuous change in our data to be the sign of a continuous transition. Well above T_m our data are consistently higher than theirs, which varies as one $k_B T$. While our data appear to increase as one $k_B T$ above $T^*=1.4$ we cannot explain the 0.5% difference in energy. We speculate that it is either an artifact of our calculation procedure or an artifact of the simulated system. A computational error, however, cannot explain the broad increase in potential energy just after melting.

The potential energy versus T^* also provides a means of calculating Γ_m, Γ at melting, without knowing the absolute magnitude of the dipole interaction. This is determined from the value of E^* at the solid-to-hexatic transition, 0.815 ± 0.001, and the assumption of a constant specific heat of k_B for the potential energy from $T=0$ to $T=T_m$. The value of E^* at $T=0$ is 0.7985. Since the difference in potential energy from its zero-temperature value to its melting value is

$$E(T=T_m)-E(T=0)=k_B T_m \ , \tag{4.1}$$

Γ_m can be calculated simply by dividing this equation by the pair potential at the Wigner-Seitz radius and then taking the reciprocal,

$$\Gamma_m = V(r_s)/k_B T_m = V(r_s)/[E(T_m)-E(0)] = 1/[E^*(T_m)-E^*(0)] \ . \tag{4.2}$$

This yields $\Gamma_m = 1/(0.8150-0.7985)$ or 61 ± 3. Kalia and Vashishta[12] report a value of 59–65 for their 2D dipole simulation. In Appendix A we find a value of 40 at the Kosterlitz-Thouless stability limit, Eq. (1.1). This calculation does not include renormalization of the elastic constant. Renormalization will increase the calculated value of Γ_m.

The slope of the data away from the transition also indicates the value of Γ_m. From the equipartition theorem, the potential-energy contribution to total energy of a harmonic system in two dimensions is one $k_B T$. In Figs. 5 and 11, where temperature is normalized to the melting temperature, the slope of one k_B is equal to $1/\Gamma_m$. The dashed lines on both graphs show a slope of k_B for $\Gamma_m = 61$. That the data for the 1.6-μm system at high temperature (above $T^* = 1.4$) apparently follow this slope is another indication that Γ_m is about 61.

The E^* vs T^* data in Fig. 11 from the 2.0-μm particles are complicated by the discrete changes in applied voltage throughout the experiment. The data do not evolve continuously, but rather are clumped together. However a trend in the data is evident. Before and after the transition, where the energy increases by 0.005, the data increase with a slope of less than k_B. The slope below T_m probably indicates that the system was not quite in equilibrium. Defects frozen into the crystal fix E^* at almost a constant value. Above T_m, the low slope indicates that the interparticle potential scales as less than the square of the applied field. This means that the interparticle potential at high temperature, or low field, is actually higher than calculated and should be shifted to the left on Fig. 11. Since the field is fixed for the 1.6-μm spheres, they are not affected by this.

This problem of reduced interaction at high fields is also manifested by the raw calculation of Γ at the hexatic-to-fluid transition. Assuming there is no screening of the applied field from ions in the water, Γ can be calculated using Eq. (2.3). For a fixed volume fraction, the field required to reach a given Γ should scale inversely as the particle radius to the $\frac{3}{2}$ power, requiring higher fields for smaller particles. The raw values of Γ for 1.6-, 2.0-, and 2.2-μm spheres at the hexatic-to-isotropic transition are 180, 80, and 50, respectively.[41] Part of this increase for small particles can be attributed to the higher ion concentration in the water due to the higher surface-to-volume ratios in the small sphere systems (with fixed volume fraction). We believe part of the increase is also a sign of the nonlinearity of the induced dipole moment in colloidal systems.

For the 1.6-μm sample the potential energy increases rapidly just above the melting point as free dislocations enter the lattice and dislocation pairs proliferate. The defects weaken the lattice constants causing the energy per defect (non-sixfold-coordinated particles) to decrease at a defect density of $\sim 5\%$. The potential energy then rises much less rapidly with effective temperature. As the defects become more dense in the fluid phase, at a density of $\sim 20\%$, the energy per defect again increases, possibly resulting from the fact that addition of more defects requires a rearrangement of existing defects, and the defect density increases more slowly with T^*. Above this temperature, $T^* \sim 1.4$, the potential energy increases by one k_B per degree.

From Fig. 6 we observe that the dislocation pair density, with four defects per pair, in the lattice phase is in the range of 0.3–0.9 %. We give a crude estimate of the dislocation core energy from these data. Fisher, Halperin, and Morf[40] calculated the density of dislocation pairs with separations larger than $r_{\min} = 3a_0$ as

$$n_{dp} = Z(\bar{K}) e^{-2E_c/T} \ , \tag{4.3}$$

Here a_0 is a lattice spacings, $Z(\bar{K}) \sim (r_{\min})^{-2}$ is the internal partition function of a dislocation pair, and $\bar{K}(T)$ is the renormalized coupling constant which is equal to 16π at $T_{\rm KT}$. Most of the pairs which we observe in the crystal phase are separated by at least two lattice spacings. We adapt the expression for $Z(\bar{K})$ from Ref. 40 for $r_{\min} = 2a_0$, which gives $Z = 45$ at $T_{\rm KT}$. This gives a core energy of $4.5 \pm 2 T_{\rm KT}$. This estimate is an approximation in part because our sample was in quasiequilibrium in the crystal phase. The ratio $E_c/T_{\rm KT}$ is larger than the value of 2.84 at which Chui[6] found a transition from a strong ($E_c/T_{\rm KT} < 2.84$) to a weak first-order transition. Saito[42] also found a continuous transition in an ensemble of dislocation vectors with high core energies. Our value of $E_c/T_{\rm KT}$ is comparable to the values deduced by Murray and co-workers[21,22] and Tang *et al.*[24] Our estimates may involve different values of $Z(\bar{K})$.

The equilibration time for this system must be considered to judge the validity of these data in exploring the melting transition in two dimensions. In both experiments, the monolayer initially was confined by glass coverslips separated by a few (2–3) particle diameters. With this setup, the monolayer formed a close-packed multicrystalline solid (with ~ 1.1 particle diameter lattice spacing) consisting of crystallites about 30 lattice spacings in extent. The monolayer was allowed to sit in this state for about an hour before the coverslip spacing was closed down to 1.5 particle diameters. The monolayer retained its order, but expanded to a lattice spacing of about two particle diameters. It was from this state that the field was applied, causing the crystal to expand and ultimately melt.

Equilibrium in the solid phase near melting is attained when a dislocation climbs the mean distance between pairs. Dislocation glide occurs on a much shorter time scale. Climb occurs when the length of a half row of atoms is altered and is usually assumed to require the creation or annihilation of vacancies or interstitials. Another mechanism to attain climb equilibration is via the diffusion of dislocation pairs from the edge of the sample. These pairs can enter with a distribution of

climb separations. We propose that the distribution of climb separations can also be altered in collisions between dislocation pairs. Collisions result either in the exchange of partners or in the annihilation of two dislocations with the remaining dislocations forming new pairs.

In the solid phase, only one interstitial and no vacancies have been seen for both samples with a total of about 20 000 particles examined. Seshadri and Westervelt[29] also note the scarcity of vacancies in their 2D dipole system. Thus, vacancies and interstitials may not play a role in equilibrating the solid phase in a dipole system. An upper limit for the equilibration time is determined by the diffusion of pairs from the boundary of the crystal. Assuming a dislocation diffusion constant of one square lattice spacing each 10 sec, 0.1 a_0^2/sec, a dislocation would take about 9 h to glide across our sample. We also give an estimate of the time for dislocation climb by dislocation collisions which neglects dislocation interactions. We define a climb separation vector along the ith crystal axis as $\vec{c}_j^{\,i}=c_j^i\hat{i}$, where c_j^i is the number of atoms which must be added ($c_j^i>0$) or eliminated ($c_j^i<0$) to annihilate dislocation pair j when partners are not separated in the glide direction, and $\hat{i}$ is a unit vector which is directed along one of the three crystalline axes. The climb separation vector is perpendicular to the Burgers vectors of the pair. The climb diffusion constant is given by

$$D=\omega\lambda^2 f\sigma p \ , \tag{4.4}$$

where ω is the dislocation glide attempt frequency, λ is the average value of $|\vec{c}_j^{\,i}|$, which we estimate to be three, $f=\frac{1}{3}$ enters because only pairs with climb vectors aligned along the same axis can collide, σ is the cross section given in rows, estimated to be about the average climb separation of a pair, and p is the probability that an exchange or annihilation event occurs in a collision. Given the density of dislocation pairs of about 0.005, the climb diffusion constant becomes $\sim 5a_0{}^2$/h, and the time to climb a correlation length is greater than 20 h. In both samples the crystal phase existed for only about 1 h before it melted. These rough estimates show that the defects in the solid phase are approximately frozen into the position determined by the initial state. However, after melting, when the density of defects increases by about an order of magnitude, this equilibration time should drop about two orders of magnitude to about 10 min due to the reduction in the average separation between dislocations and the availability of defects to promote dislocation climb. We feel that these estimates support our position that although the solid phase was not in equilibrium, as soon as defect concentrations increased to about 5%, the time scale of our experiment was sufficient to allow for equilibrium. We contend that the later stages of the hexatic phase and all of the liquid phase are in equilibrium.

Finally, we make one additional comment on the need of crystal boundaries for equilibration. It should be noted that dislocation climb involving only pair collisions, vacancies and interstitials imposes an additional constrain on the system. The sum of the climb vectors along a single axis is equal to an integer c^i; $\sum c_j^i=c^i$. In the interior of the crystal dislocation pairs are created with $c_j^i=0$, and creation and annihilation events do not contribute to the sum. The value of the integers, c^i, can be altered by the absorption or emission of vacancies and interstitials. If defects are not created and annihilated at crystal boundaries, the following constraint is imposed on the sample:

$$\sum_{i=1}^{3} c^i+N_V-N_I=k \tag{4.5}$$

where N_V and N_I are, respectively, the total number of vacancies and interstitials, and k is a constant. Crystal boundaries are essential in obtaining true equilibrium.

V. CONCLUSIONS

The melting of a lattice of colloidal spheres with dipole interactions which could be controlled externally was reported. Melting occurred in two stages with an intermediate hexatic phase. Long equilibration times in the crystal phase limited this phase to a quasiequilibrium state. Lack of equilibrium could possibly be a cause of the apparent continuous nature of the first melting transition. While we cannot rule out a weak first-order transition from the solid to the hexatic phase, we observe clear evidence of a continuous transition to the fluid phase. The defect structures for the three phases were consistent with predictions of the KTHNY theory of melting. The melting point at $\Gamma=61\pm3$ matched the value from simulations of heating a lattice with dipole interactions. The width in temperature of the hexatic phase was 15% of T_m. Melting occurred when the algebraic decay exponent for the translational correlation function was near the predicted value of $-\frac{1}{3}$ although a precise value was difficult to obtain due to quasiequilibrium conditions. The second transition occurred when the algebraic exponent for the bond-orientational correlation function reached the predicted value of $-\frac{1}{4}$ where the function abruptly changed from algebraic to exponential decay.

The first measurements of potential energy and defect density versus effective temperature were presented. The potential energy as determined from the experimental data varied smoothly through both the transitions with a rapid rise in energy just above the melting point. The variation of defect density was smooth, but the reduced energy per defect was nonmonotonic. Our results are similar to the beautiful experiments by Murray and coworkers and Tang *et al.* on colloidal spheres with a screened Coulomb interaction.

ACKNOWLEDGMENTS

We wish to acknowledge the contributions of M. E. Glinsky, J. A Mann, III, and A. Tatah to an earlier version of this project, the valuable assistance of W. J. Benton, J. Kerins, and H. Nguyen, and discussions with A. J. Armstrong, N. A. Clark, C. A. Murray, R. G. Petschek, Y. Tang, and D. J. Thouless. This work was supported in part by The Petroleum Research Fund, a grant from BP America, and NSF Grant No. DMR-9100242.

APPENDIX: CALCULATION OF ELASTIC CONSTANTS FOR A TRIANGULAR LATTICE

Below, we present the calculation of the elastic constants for a 2D lattice in a compressed state. The usual presentation assumes a relaxed state for the solid. We allow for an intrinsic spreading pressure. The result specific to a 2D dipole lattice is given.

Following the work of Born and Huang[43] the pair potential is expanded in a Taylor series about the square of the pair separation. To quadratic order, the energy density is given by

$$U=\frac{1}{\nu_a}\left\{\sum_{ij}\left[u_{ij}+\sum_k u_{ki}u_{kj}\right]\sum_r{}'[\phi'(r^2)r_i r_j] + \sum_{ijkl}u_{ik}u_{jl}\sum_r{}'[\phi''(r^2)x_i x_k x_j x_l]\right\}, \tag{A1}$$

Here the prime indicates that the summation does not include the origin, ν_a is the atomic volume, $\phi(r^2)$ is the interparticle potential, presented above with first and second derivatives taken with respect to r^2, and the displacements tensor, u_{ij}, is the gradient of the displacement vector,

$$\mathbf{u}_{ij}=\partial \mathbf{u}_i/\partial \mathbf{r}_j \tag{A2}$$

The term in equation (A1) linear in u_{ij} describes the effects of intrinsic stress on the system. In the event that its coefficient,

$$p_{ij}=\frac{1}{\nu_a}\sum_r{}'\phi'(r^2)r_i r_j , \tag{A3}$$

in zero, only the final term of (A1) remains. This final term can be symmetrized to produce that elastic free energy written in terms of the strain tensor.

If the intrinsic stress is not zero, the system is only stable if there is an external, equalizing stress. A simplification occurs if these stresses are isotropic and homogeneous. In this case the equilibrium is determined by the Gibbs free energy,

$$G=F+pV=G_0+p\Delta V . \tag{A4}$$

The change of volume is equal to

$$\Delta V=V_0|\delta_{ij}+u_{ij}|-V_0 , \tag{A5}$$

where δ_{ij} is the identity tensor and u_{ij} is the displacement tensor, given by (A2). Applying the result to (A1) yields

$$G=\frac{1}{2\nu_a}\sum_{ijkl}u_{ik}u_{jl}\left\{2\sum_r{}'[\phi''(r^2)r_i r_j r_k r_l] - \nu_a p(\delta_{ij}\delta_{kl}-\delta_{ik}\delta_{jl}+\delta_{il}\delta_{jk})\right\}, \tag{A6}$$

where p is the hydrostatic pressure, which in two dimensions, is equal to half the trace of (A3), the intrinsic stress tensor. The above energy can be symmetrized to form the familiar elastic free energy with elastic constants

$$\lambda=\frac{1}{4\nu_a}\sum_r{}'[r^4\phi''(r^2)]-\frac{1}{2}\sum_r{}'[r^2\phi'(r^2)] , \tag{A7}$$

and

$$\mu=\frac{1}{4\nu_a}\sum_r{}'[r^4\phi''(r^2)]+\frac{1}{2}\sum_r{}'[r^2\phi'(r^2)] . \tag{A8}$$

The above results are applied to an inverse cube potential. Assuming a potential of the form

$$\phi(r^2)=p^2/(r^2)^{3/2} , \tag{A9}$$

the expressions for the two elastic constants given above become

$$\lambda=\frac{27}{16\nu_a}\frac{p^2}{a^3}\sum_r\frac{a^3}{r^3} , \tag{A10}$$

and

$$\mu=\frac{3}{16\nu_a}\frac{p^2}{a^3}\sum_r\frac{a^3}{r^3} , \tag{A11}$$

where a is some length such as the lattice spacing. If a is the lattice constant, the sum has the value 11.033 for a triangular lattice. Parametrizing the results in terms of $k_B T\Gamma$, in which Γ is defined as

$$\Gamma=\phi(1/\pi n)/k_B T , \tag{A12}$$

and where n is the 2D number density of the lattice, yields the following expressions for the elastic constants in a 2D triangular lattice with a dipole potential:

$$\lambda=2.695\Gamma k_B T/\nu_a , \tag{A13}$$

and

$$\mu=0.2994\Gamma k_B T/\nu_a . \tag{A14}$$

Applying these results to the Kosterlitz-Thouless stability criterion yields an unrenormalized value for Γ at melting:

$$\Gamma_m=40.0 . \tag{A15}$$

*Present address: NASA Lewis Research Center, Cleveland, OH 44135.

[1]J. M. Kosterlitz and D. J. Thouless, J. Phys. C. **6**, 1181 (1973).
[2]B. I. Halperin and D. R. Nelson, Phys. Rev. Lett. **41**, 121 (1978); D. R. Nelson and B. I. Halperin, Phys. Rev. B **19**, 2457 (1979).
[3]A. P. Young, Phys. Rev. B **19**, 1855 (1979).
[4]N. D. Mermin, Phys. Rev. **176**, 250 (1968).
[5]A. N. Berker and D. R. Nelson, Phys. Rev. B **19**, 2488 (1979).
[6]S. T. Chui, Phys. Rev. Lett. **48**, 933 (1982); Phys. Rev. B **28**, 178 (1983).
[7]T. V. Ramakrishnan, Phys. Rev. Lett. **41**, 541 (1982); T. V. Ramakrishnan and M. Yussouf, Phys. Rev. B **19**, 2775 (1979).
[8]H. Kleinert, Phys. Rev. Lett. **95A**, 381 (1983).

[9]M. A. Glaser and N. A. Clark, Phys. Rev. B **41**, 4585, (1990); M. A. Glaser, N. A. Clark, A. J. Armstrong, and P. D. Beale, in *Dynamics and Patterns in Complex Fields,* edited by A. Onuki and K. Kawasaki (Springer-Verlag, Heidelberg, 1990), p. 141.

[10]M. A. Glaser and N. A. Clark, in *Advances in Chemical Physics,* edited by I. Prigogine and S. A. Rice (Wiley, New York, 1993), Vol. 83, p. 543.

[11]K. J. Strandburg, Rev. Mod. Phys. **60**, 161 (1988).

[12]R. K. Kalia and P. Vashishta, J. Phys. C **14**, L643 (1981).

[13]V. M. Bedanov, G. V. Gadiyak, and Y. E. Lozovik, Phys. Lett. **92A**, 400 (1982).

[14]V. M. Bedanov, G. V. Gadiyak, and Y. E. Lozovik, Zh. Eksp. Teor. Fiz. **88**, 1622 (1985) [Sov. Phys. JETP **61**, 967 (1985)].

[15]The value of $0.32k_B$ from Ref. 13 is taken from their Fig. 8.

[16]C. A. Murray, in *Bond-Orientational Order in Condensed Matter Systems,* edited by K. J. Strandburg (Springer-Verlag, New York, 1992), p. 137.

[17]G. Deville, A. Valdes, E. Y. Andrei, and F. I. B. Williams, Phys. Rev. Lett. **54**, 1710 (1985).

[18]D. C. Glattli, E. Y. Andrei, and F. I. B. Williams, Phys. Rev. Lett. **60**, 420 (1988).

[19]H. W. Jiang and A. J. Dahm, Surf. Sci. **229**, 352 (1990).

[20]M. A. Stan and A. J. Dahm, Phys. Rev. B **40**, 8995 (1989).

[21]C. A. Murray and D. H. Van Winkle, Phys. Rev. Lett. **58**, 1200 (1988).

[22]C. A. Murray and R. A. Wenk, Phys. Rev. Lett. **62**, 1643 (1989); C. A. Murray, W. O. Sprenger, and R. A. Wenk, Phys. Rev. B **42**, 688 (1990).

[23]A. J. Armstrong, R. C. Mockler, and W. J. O'Sullivan, J. Phys. Condens. Matter **1**, 1707 (1989).

[24]Y. Tang, A. J. Armstrong, R. C. Mockler, and W. J. O'Sullivan, Phys. Rev. Lett. **62**, 2401 (1989); Phase Transitions **21**, 75 (1990).

[25]N. Geiser, G. A. Held, R. Frahm, P. L. Greene, P. M. Horn, and R. M. Suter, Phys. Rev. Lett. **9**, 1706 (1987).

[26]A. D. Migone, Z. R. Li, and M. H. W. Chan, Phys. Rev. Lett. **53**, 810 (1984); A. J. Jin, M. R. Bjurstom, and M. H. W. Chan, *ibid.* **62**, 1372 (1989).

[27]A. T. Skjeltorp, Phys. Rev. Lett. **51**, 2306 (1983).

[28]G. Helgesen, and A. T. Skjeltorp, Physica A **170**, 488 (1991).

[29]R. Seshadri and R. M. Westervelt, Phys. Rev. Lett. **66**, 2774 (1991); Phys. Rev. B **46**, 5142 (1992).

[30]R. E. Kusner, Ph.D. thesis, U.M.I., 1993.

[31]R. E. Kusner, J. A. Mann, J. Kerins, and A. J. Dahm, Phys. Rev. Lett. **73**, 3113 (1994).

[32]Interfacial Dynamics, Inc., Portland, OR, 97220.

[33]J. Vig, J. Vac. Sci. Technol. A **3**, 1027 (1985).

[34]A. J. Armstrong, Ph.D. thesis, University of Colorado, 1988.

[35]J. D. Jackson, *Classical Electrodynamics,* 2nd ed. (Wiley, New York, 1975), p. 152. It should be noted that p is the source of the displacement field, and not necessarily the coefficient of the dipole term in the potential expansion.

[36]F. P. Preparata and M. L. Shamos, *Computational Geometry, an Introduction* (Springer-Verlag, New York, 1985), p. 198; D. T. Lee and B. J. Schachter, Int. J. Comput. Info. Sci. **9**, 219 (1980).

[37]Although the procedure constitutes the definition for a continuum function, the interpolated values are computed only at regularly spaced, discrete points, i.e., a 512×512 complex array with the same resolution as the digitized image.

[38]W. H. Press, B. P. Flannery, S. A. Tuekolsky, and W. T. Vetterling, *Numerical Recipes* (Cambridge University Press, Cambridge, 1986), p. 381.

[39]W. H. Press, *Numerical Recipes* (Ref. 38), p. 410.

[40]D. S. Fisher, B. I. Halperin, and R. Morf, Phys. Rev. B **20**, 4692 (1979).

[41]R. E. Kusner, J. A. Mann, and A. J. Dahm, Phys. Rev. B **49**, 9190 (1994).

[42]Y. Saito, Phys. Rev. Lett. **48**, 1114 (1982); Phys. Rev. B **26**, 6239 (1982).

[43]M. Born and K. Huang, *Dynamical Theory of Crystal Lattices* (Oxford University Press, London, 1954), p. 129.